Investigation of Failure Processes in Porous Battery Substrates: Part I—Experimental Findings

C. Wang

X. Cheng

A. M. Sastry

S. B. Choi

Department of Mechanical Engineering and Applied Mechanics, The University of Michigan, Ann Arbor, MI 48109-2125

Experimental findings are presented which demonstrate the coupled transport, mechanical and morphological changes in porous battery materials when they are cycled electrochemically. These materials, comprised of a mixture of powdered nickel and nickel fiber, act as substrates in nickel-metal hydride (NiMH) cells, and function as porous, conductive containment for positive-plate active material. They can offer substantial weight and cost savings over more traditional sintered or foam materials, provided they can be designed to produce good conductivity over many (>500) electrochemical cycles. This study represents an expansion of previous work by the authors, which had established some key differences in the behavior of substrate materials for a small number of cells. Here, these differences are validated with a greater variety and number of electrochemical/material experiments, along with a parallel study on morphological changes. In the second paper in this series (Cheng et al., 1999b), transport and mechanics models are presented to explain the observed differences, using microstructural models based on observations in this study.

I Introduction

The advancement of many power storage technologies hinges on development of inexpensive and reliable materials to allow improved energy density, lifetime and cost. Production of marketable zero-emission vehicles (ZEV's) depends in large measure on the availability of high energy density, long life and affordable automotive batteries to power electric motors. Nickel-metal hydride (NiMH) cells offer critical combinations of energy density and lifetime which has made them an attractive technology for vehicles. Improvement in performance of these cells remains a central goal of battery and automobile manufacturers. Improvement to design of positive plate substrates in NiMH cells are the focus of the present work.

The current work represents an expansion of an earlier experimental study, which established several key differences in material behavior in cycled and uncycled cell materials (Sastry et al., 1998). Here, plate and substrate compression are also studied, and an additional material is considered. Expanded mechanical and resistivity experiments are also described, as suggested from results of prior work. In the second paper in this series (Cheng et al., 1999b), simulations are described to explain the observations here, and guidelines are suggested to improve substrate performance.

Function and Composition of NiMH Positive Plates. The NiMH cell reaction, shown schematically in Fig. 1(*a*), is positive-limited, i.e., the reactant mass on the positive plate limits cell capacity. The plate itself (shown in Fig. 1(*b*)) is comprised of two distinct components: the substrate, consisting of an open metallic (conductive) grid, and the active material paste, containing the chemical reactants in Fig. 1(*a*). The conductive grid, or substrate, is a porous nickel plate. The active material paste is rolled or vacuum impregnated into the substrate and dried to form the positive plate.

The assembled cell is produced by covering the positive plate with separator material, and immersing the contents (positive and negative plates as shown in Fig. 1(*c*) in electrolytic fluid in the enclosed cell. The cell is compressed in the cell case to assure good contact of all reactive surfaces. The compression used (or the gage thickness to which the assembled cell is tightened, per Fig. 1(*c*), is usually developed empirically (Muller, 1997); dimensions in the figure reflect those used in experiments described later.

Positive plate substrates are generally comprised of porous nickel, either in the form of a sinter or a foam. Random-fiber architecture substrates (e.g., material shown in Fig. 1(*d*)), have also been shown to be a cost-effective morphology. Ferrando, Lee and Sutula (1984), first examined the use of fibrous substrates, in the form of a graphite fiber structure coated with sintered nickel. Coates et al. (1990) later performed experiments on non-woven nickel fiber and powder (National Standard Fibrex material) substrates, and sintered powder materials, and showed that fibrous electrodes exhibited greater utilization while showing a smaller impedance gain when compared to a sinter material. Results suggested that fibrous materials could be developed to provide more power over the discharge curve due to its dimensional stability versus the sintered powder. Tatarchuk, et al. (1994) investigated the use of standard wet paper-making processes to create conductive materials. They concluded that fibrous materials made of mixed and dissimilar materials could exhibit properties which were thought to be exclusive to each separate material in the mixture.

A previous study by the current authors (Sastry et al., 1998) revealed that material properties in the compressed cell condition (as they are typically used in practice) exhibited different trends than materials in the uncompressed condition. Though resistivity was increased (accounting for the dimensional change due to cycling by consideration of the new dimensions in calculations), secant modulus and peak stress of dry substrate materials increased with cycling. The hypothesis of local failures in the material causing loss of connectivity would be consistent with observed transport (electrical conduction) losses, but inconsistent with the observations of increased mechanical properties, in the absence of other strengthening and stiffening phenomena. The present study was undertaken to explain these effects in total.

Contributed by the Materials Division for publication in the JOURNAL OF ENGINEERING MATERIALS AND TECHNOLOGY. Manuscript received by the Materials Division February 17, 1999; revised manuscript received June 25, 1999. Guest Editors: Assimina A. Pelegri, Ann M. Sastry, and Robert Wetherhold.

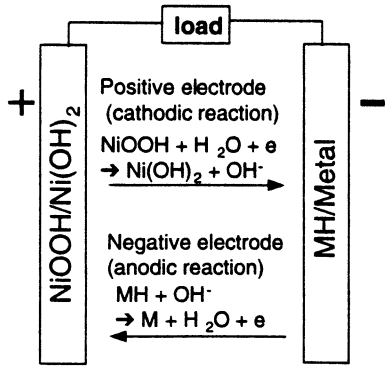

Fig. 1(*a*)

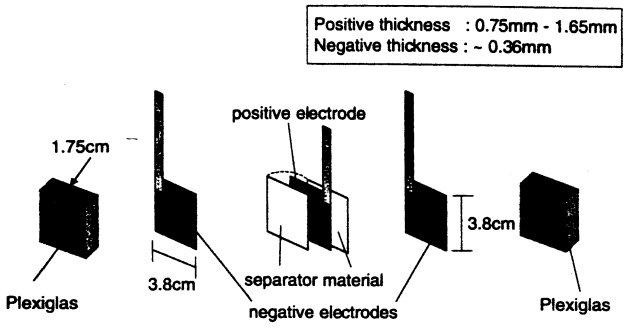

Fig. 1(*b*)

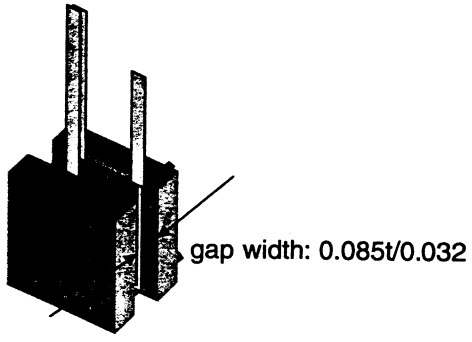

Fig. 1(*c*)

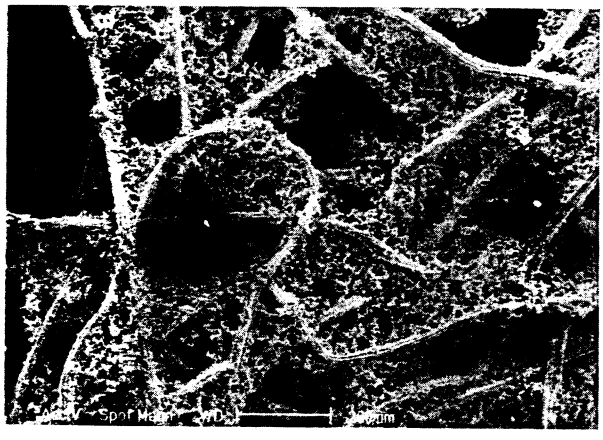

Fig. 1(*d*)

Fig. 1 (*a*) The electrochemical reaction in a Ni/MH cell. (*b*) Schematic with dimensions of a test cell (~0.2–0.5 Ah batteries) used in this study. (*c*) Assembled cell with gage thickness shown, and (*d*) Scanning electron micrograph of a positive plate substrate (National Standard 5% AFS).

Specific energy (capacity per unit mass, with typical dimensions Wh/kg) is a critical design parameter in automotive cells, as additional mass reduces almost all important indicators of vehicle performance (e.g. acceleration, braking distance, rolling friction, etc.). The positive electrode substrate mass alone accounts for a significant portion of the overall battery mass in the NiMH cell, comprising approximately 35% of the cell's overall mass, even for the low-density fibrous structures studied (Hellen, 1999). Thus, reduction of substrate mass is an important design goal in battery manufacture, driving investigation of use of highly porous structures such as the random fiber substrates studied here. The requirements of low mass and open microstructure must be balanced by the need for high electrical conductivity in the positive plate substrate. Good conductivity is required to assure completion of ion transfer on the positive plate; loss of conductivity in the substrate results in reduction of capacity, and ultimately, reduced lifetime of the cell; this general class of morphologies and their conductivities have been studied in detail by the current authors (e.g., Sastry, 1994; Sastry et al., 1998; Cheng and Sastry, 1999; Cheng et al., 1999a).

Material Changes in the Positive Substrate: Previous Observations. Lower density chemical species are formed irreversibly in the active material on the positive plate during operation of a NiMH cell. Specifically, formation of γ-NiOOH phase is formed as a byproduct of the charge cycle. This γ-NiOOH phase is of lower density than other nickel species. Thus, its formation causes mechanical swelling in the active material in the positive plate, loading the substrate network and expanding the cell thickness. This has been hypothesized to result in mechanical fatigue of the electrode, limiting cell lifetime. This has been observed in sintered nickel substrates by a number of workers (e.g., Fritts, 1981; Oshitani et al., 1986). Efforts to reduce the effects of swelling for NiMH automotive cells include the commonly-performed commercial technique of mechanical banding of the cell to resist swelling, for all types of substrates in the positive plate. Several reactants have also been shown empirically to inhibit production of the γ-NiOOH, but the addition of such reactants significantly increases cell cost. Cell corrosion, especially during overcharge, has also been reduced somewhat by use of additives; Oshitani et al. (1986), for example, found cobalt, cadmium, zinc, magnesium in addition to Group II elements helpful in varying degrees. Cobalt, when combined with cadmium, proved most effective in inhibiting the formation of the γ-NiOOH.

Several workers have, directly and indirectly, studied morphological changes in positive plate substrates through use of electrochemical, mechanical and transport experiments. Most of these efforts have been empirical in nature, and have focused on nickel sinters. Ettel (1991), for example, used a bending test to record absolute tensile strength for various electrode materials, and also included a simple cubic network model for failure. However, this analysis of substrate materials did not produce verifiable models linking experiments and simple mechanical models of electrode materials with performance. Davolio et al. (1989) linked reduction in substrate elastic modulus to damage resulting from the cyclic force exerted on the sinter substrate structure by the active material expanding during discharge and contracting during charge. Fritts (1984) incorporated electrode growth measurements for sintered substrates and fatigue testing with hardness measurements to examine the mechanical characteristics of sintered electrode materials. Tension fatigue experiments, were correlated to transport losses: materials with higher overall increases in resistivity during testing also showed reduced fatigue life. The results suggested that resistivity increases in the materials were due to fatigue failures of the internal sintered bonds.

High porosities have been generally linked to increased plate swelling (e.g. Coates et al., 1990) in sintered materials. The corrosive environment in NiMH cells has also been suspected of changing the mechanical properties of the electrode constituents, thus leading to changes in fibrous substrates (Ferrando, 1992).

Table 1 Material compositions of the positive plate substrate materials investigated

Designation	Manufacturer	Composition	Fiber Diameter (μm)	Staple Length (cm)	Volume Fraction (%)	Fiber/Powder Ratio
Material 1	Fibrex	97% Nickel, 3% Contaminants	30	0.635-1.27	18	50/50
Material 2	Fibrex	97% Nickel, 3% Contaminants	30	0.635-1.27	7	50/50
Material 3	AFS	99.9% Nickel	20	1.27-1.905	5	50/50

Thus, work to date has identified several technological challenges in improvement to substrate materials:

1) development of high porosity substrates with acceptable conductivity over a high number of cycles, to extend cell life,
2) development of methodologies for manufacturers to assess these characteristics for candidate materials, using reliable, predictive material proof tests, and
3) development of materials resistant to swelling.

The study here was performed to gain greater understanding of material changes in fibrous substrates during cycling under realistic operating conditions, focusing attention on the first two of these challenges. Thus, experiments were performed on as-received, compressed (to the cycling thickness) and post-cycled materials to systematically compare evolving substrate material properties. Future work addressing the third challenge is discussed in the second paper of this series.

II Experimental Methodology and Experimental Findings

Image analysis of the substrate materials (to assess microstructure), resistivity testing and mechanical testing were performed. Composition analysis was also performed for all materials in the compressed and post-cycled conditions, to verify that no contamination of materials took place during cycling, and also to allow estimation of material properties for the modeling effort (Cheng et al., 1999b). In all cases, particular attention was paid to variability in resulting measurements, since variances in mechanical and transport properties can be large for porous materials tested at a relatively small scale. Materials studied were comprised of a mixture of fibers and particles, as listed in Table 1.

Resistivity and mechanical tests were performed on substrate materials in three separate conditions: as-received, transversely compressed (without cycling, to post-cycled thickness—see Fig. 1(*c*) for compression direction) and post-cycled. Compressed materials were evaluated in order to provide a clear comparison between uncycled and post-cycled materials, with identical gross dimensions. Compression was performed with a mechanical vise, and compressed thicknesses were matched to those of post-cycled materials.

Image Analysis of Substrate Materials. The substrate materials are essentially planar sheets of particles bonded to interconnecting fibers, with random in-plane orientation, and small-to-moderate out-of-plane orientation. To verify the validity of this general characterization, detailed image analysis was performed on potted and polished specimens. This technique was used so that 2D sections could be analyzed quantitatively and unambiguously, without depth-of-field effect.

Substrate specimens were (1.27 × 1.27 cm) were imaged with a Nikon Optiphot optical light microscope outfitted with a digital camera. Digital images were processed in part using the NIH

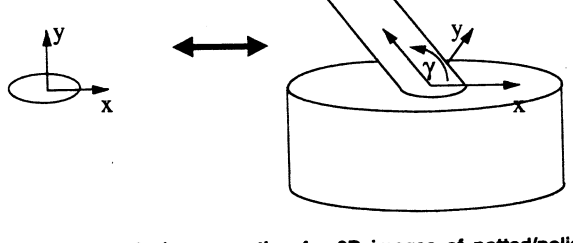

Fig. 2 Image analysis assumption for 2D images of potted/polished substrate material samples

Fig. 3(*a*)

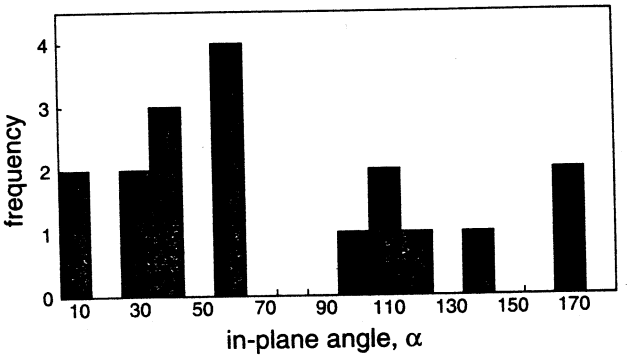

Fig. 3(*b*)

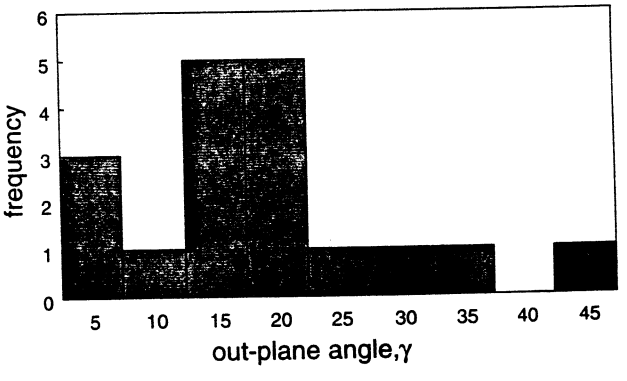

Fig. 3(*c*)

Fig. 3 Image analysis of material #1 (18% Fibrex, as-received); with (*a*) sample image field, shown with maximum contrast, and histograms of (*b*) in-plane orientation angle α, and (*c*) out of plane orientation angle γ

Image, a program from the National Institute of Health designed for medical applications, which allowed automated calculation of locations, dimensions and orientations of elliptical objects. Due to the small out-of-plane orientation of the fibers, in-plane 2D sections of the substrates were comprised of elongated, disperse elliptical inclusions. Data recorded for these elliptical fiber sections included x and y midpoints, major axis length (2D fiber section length), minor axis length (fiber diameter), in-plane angle (denoted α) and out-of-plane angle (denoted γ) and information on locations of fiber intersections. Angles α and γ were measured as shown in the schematic of Fig. 2, with γ calculated from the major and minor lengths as:

$$\gamma = 90 - \cos^{-1}\left(\frac{\text{fiber length}}{\text{fiber diameter}}\right) \quad (1)$$

Fig. 4(*a*)

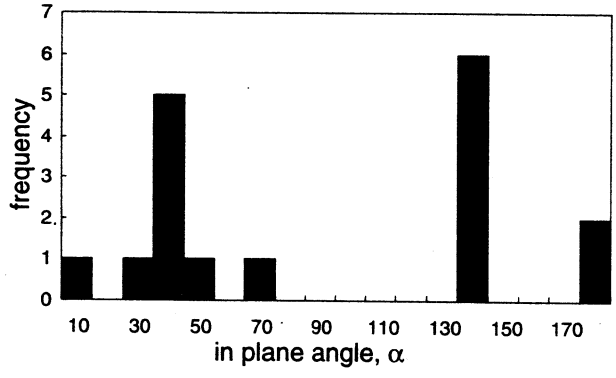

Fig. 4(*b*)

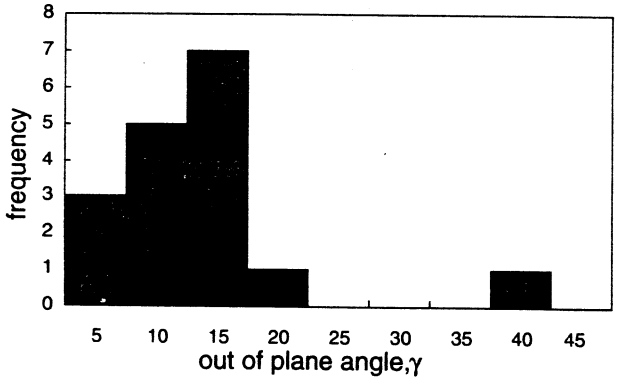

Fig. 4(*c*)

Fig. 4 Image analysis of material #2 (7% Fibrex, as-received); with (*a*) sample image field, shown with maximum contrast, and histograms of (*b*) in-plane orientation angle α, and (*c*) out of plane orientation angle γ

Fig. 5(*a*)

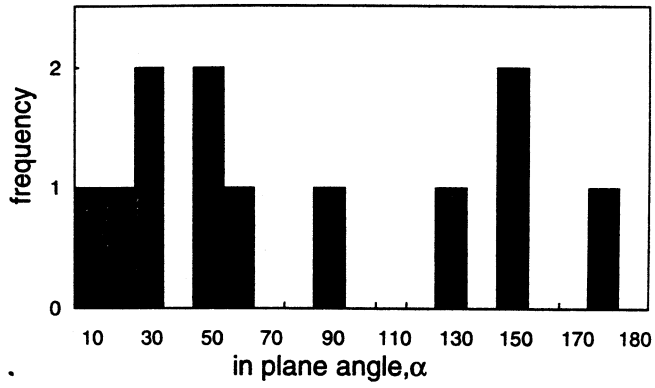

Fig. 5(*b*)

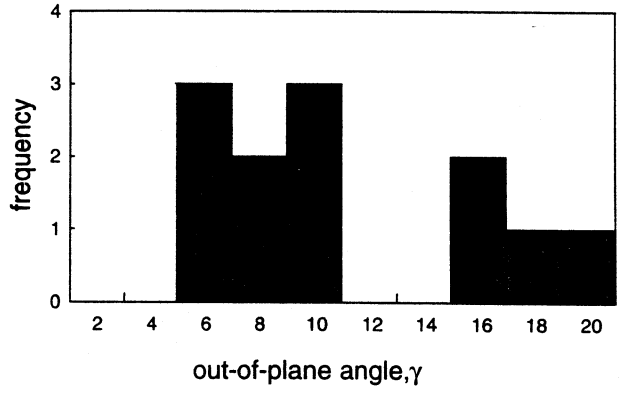

Fig. 5(*c*)

Fig. 5 Image analysis of material #3 (5% AFS, as-received); with (*a*) sample image field, shown with maximum contrast, and histograms of (*b*) in-plane orientation angle α, and (*c*) out of plane orientation angle γ

Representative results of image analysis are shown for samples of each of the material types in Table 1 (materials 1, 2, and 3 shown in Figs. 3, 4, and 5, respectively). Original images (shown at high contrast in Figs. 3(*a*), 4(*a*), and 5(*a*)) and histograms of orientations α and γ are shown in each case. Each material exhibited essentially uniform (random) in-plane fiber orientation, per histograms of α as in Figs. 3(*b*), 4(*b*), and 5(*b*), and small out-of-plane orientations of less than approximately 20 deg, per histograms of γ in Figs. 3(*c*), 4(*c*) and 5(*c*). Only large objects (i.e., fiber segments) were analyzed, since it was assumed at the outset that the particles were randomly distributed in three dimensions on the network. Quantitative image analysis was performed for only the as-received materials.

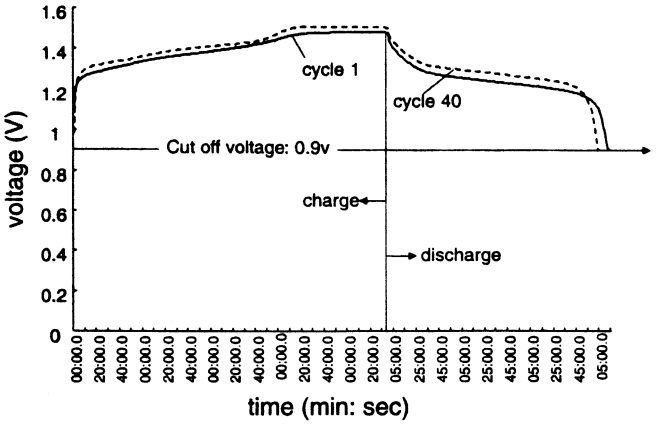

Fig. 6(*a*)

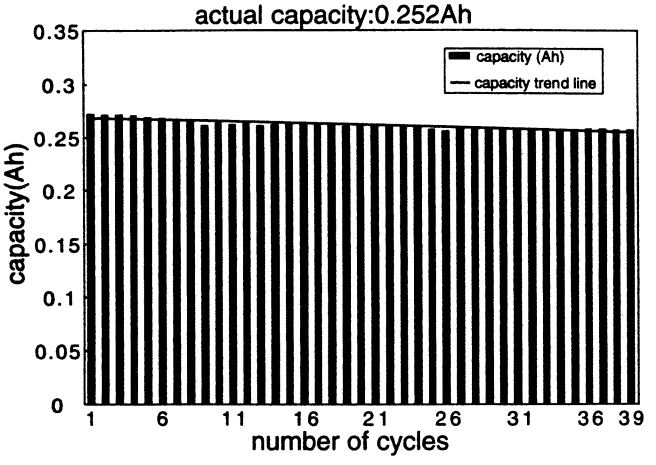

Fig. 6(*b*)

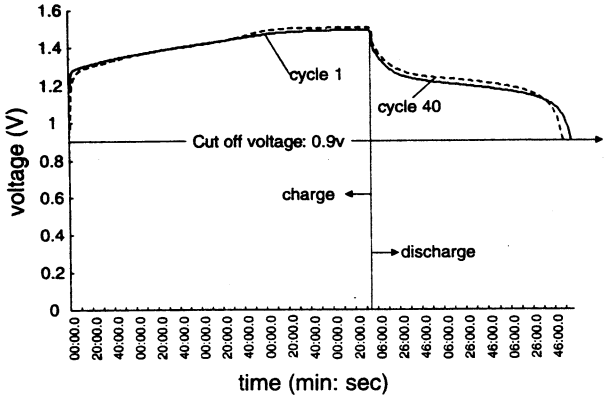

Fig. 6(*c*)

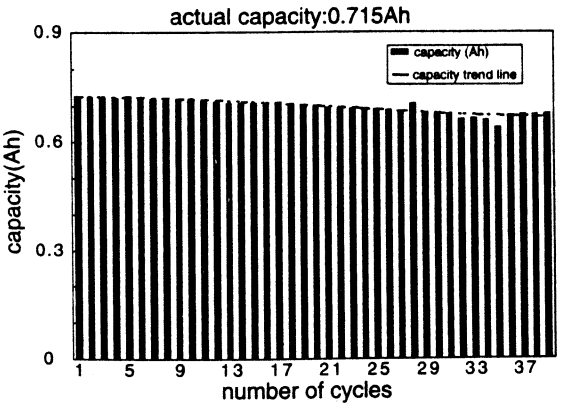

Fig. 6(*d*)

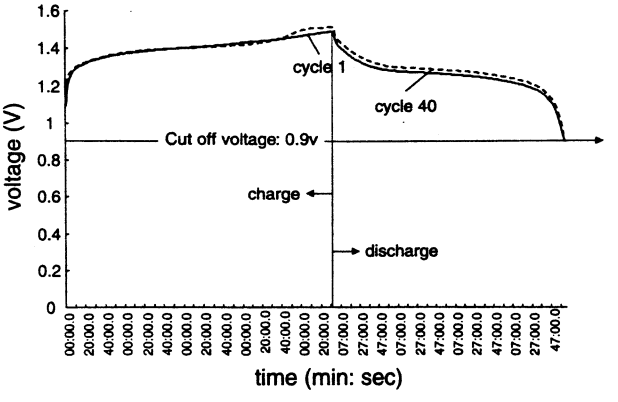

Fig. 6(*e*)

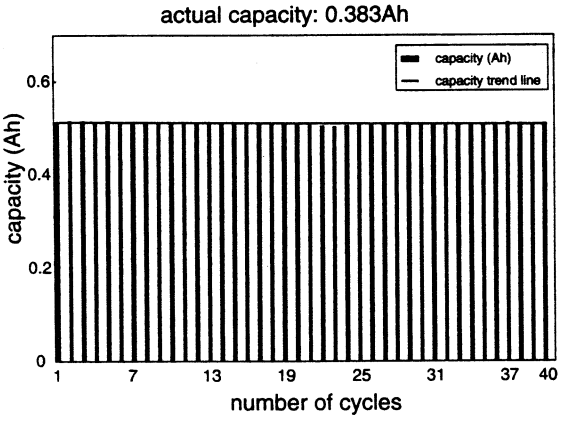

Fig. 6(*f*)

Cell Testing. Cell testing was conducted in accordance with the procedure described in Sastry et al. (1998), following guidelines established by automakers for electric vehicle batteries (USABC, 1996). The tri-electrode cells formed in this study had capacities ranging from around 0.2–0.6 Ah; positive plates were constructed of each of the substrate materials in Table 1. Cell compression was applied during all experiments, and cells were cycled in a 40-cycle constant current, 150% overcharge regimen.

Representative experimental results are shown in Figs. 6. For each material, experimental voltage versus time, and capacity versus cycle number is shown (Figs. 6(*a*)–6(*f*)). Averaged capacity losses are compared in Fig. 6(*g*). As shown in these figures, capacity losses were more severe in the higher density substrates; variances were relatively high. No batteries were cycled beyond approximately 85% depth-of-discharge (DOD).

Post-cycled substrate materials were recovered from the positive plates (Fig. 7), and deloaded, i.e., active material was chemically removed, without further dimensional change to the material. Cell compression (Fig. 1(*c*)) resulted in a reduction in thickness of post-cycled versus as-received material specimens. This reduction in thickness was acceptably uniform within each material type.

Resistivity Testing. Previous resistivity measurements had been performed with an eight-probe apparatus (Fig. 8(*a*)), adapted from ASTM standards for testing resistivity of thin films. While

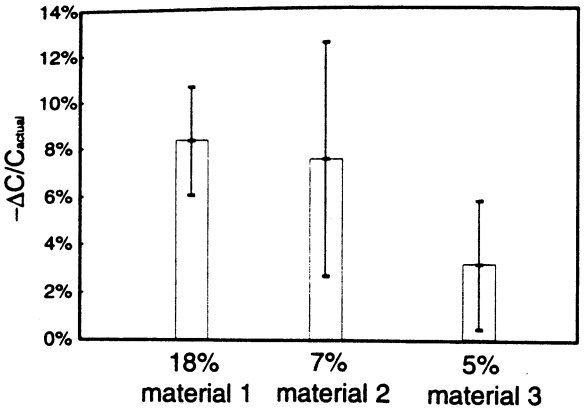

Fig. 6(*g*)

Fig. 6 Charge/discharge profiles, showing voltage vs. time, and cell capacity versus cycle, respectively, for representative cells with positive plate substrates comprised of (*a*)–(*b*) material #1, (*c*)–(*d*) material #2, and (*e*)–(*f*) material #3. A comparison of capacity losses (with $\pm 1\sigma$ standard deviation shown) is shown in (*g*).

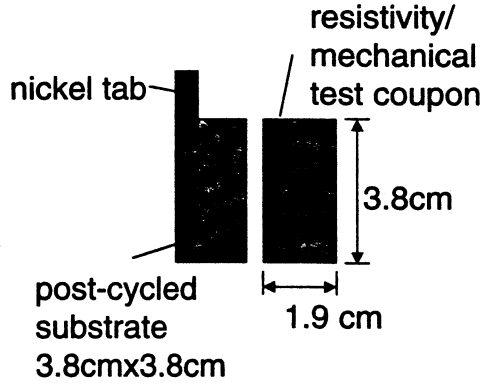

Fig. 7 Schematic of test coupons cut from post-cycled battery substrates. Each test cell contains a single positive plate, which is deloaded and cut into the specimens as shown.

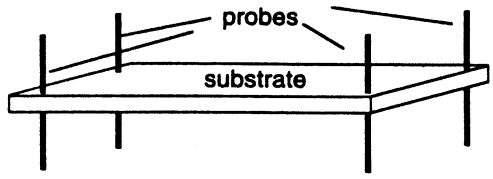

Fig. 8(*a*)

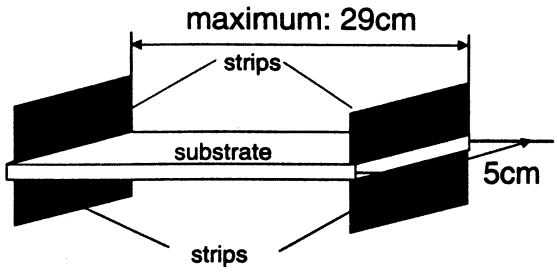

Fig. 8(*b*)

Fig. 8 Schematic of test apparatus for measurement of resistivity. An (*a*) eight point fixture was initially used, later replaced by (*b*) a strip configuration, which produced more stable results. 100

results for resistance stabilized over time, better results were obtained with strip contacts (Fig. 8(*b*)). Results from the two methods differed essentially only in time required for resistance values to stabilize (the probe method produced fluctuating resistance values about a similar mean to the strip method). Results for all materials, for the three conditions studied, are shown in Table 2, along with volume fractions in each condition, for each material type.

Resistivity decreased substantially for all materials after simple compression, somewhat beyond what would be expected via closed-form predictions for change in effective properties with increase in volume fraction. This is characteristic of materials near the percolation threshold for conduction: compression acts to nonlinearly increase bond density, so that increase on conductivity is disproportionately high. These geometries have been successfully modeled using 2D approaches, which can be viewed as valid for fixed thicknesses when fibers are oriented at relatively small out-of-plane angles (for more discussion, see Cheng and Sastry, 1999; Cheng et al., 1999a).

Post-cycled materials showed significantly higher resistivities than uncycled materials of the same thickness ("compressed" samples, in Table 2), with higher overall increases in the densest material.

Mechanical Testing. Secant moduli and peak stresses were measured for all materials in the three conditions previously described. The test procedure was adapted from ASTM D 828-93 for paper and paperboard. Post-cycled materials were tested using a single specimen size (see Fig. 7) due to the small size of the experiments and long term of each experiment (~2 weeks per cell); several sizes of specimens were used for the as-received materials, however, to verify that there was not a strong sizes effect over a practical range of material sizes. Additional strain rates were also used in this study over previous studies, to verify that strain rates in a relevant technological range (suggested by estimated strain rates in deformation of cells in work by Oshitani, 1986) did not produce dramatically different results; results reported in Table 2 were obtained with strain rates of 0.0006 sec^{-1}. Representative results are shown for materials 1, 2, and 3 in Figs. 9(*a*), (*b*), and (*c*), respectively. The highest volume fraction material, exhibited some apparent stiffening at medium strain rate, but the results for strain-rate dependent moduli and peak load were within measured variances over several experiments. The shape of the stress-strain curves in each condition was very consistent, regardless of the strain rate in the range examined.

Shape, secant moduli and peak loads differed significantly, however, among as-received materials, compressed materials and

Table 2 Overall resistivities, stiffnesses and strengths measured for materials tested in as-received, compressed and post-cycled conditions

Parameter	Resistivity (μΩ•cm)			Initial Modulus(MPa)			Peak Stress(MPa)		
Condition	As Received [vf, %]	Compressed [vf, %]	Post-cycled [vf, %]	As Received [vf, %]	Compressed [vf, %]	Post-cycled [vf, %]	As Received [vf, %]	Compressed [vf, %]	Post-cycled [vf, %]
Material 1	87 [18]	78 [29]	89 [29]	1406 [18]	1416 [29]	2144 [29]	8.613 [18]	13.05 [29]	15.82 [29]
Material 2	513 [7]	175 [14]	306 [14]	315.9 [7]	507.7 [14]	622.3 [14]	2.078 [7]	4.286 [14]	5.550 [14]
Material 3	545 [5]	193 [10]	323 [10]	199.0 [5]	197.4 [10]	310.5 [10]	1.748 [5]	2.723 [10]	2.862 [10]

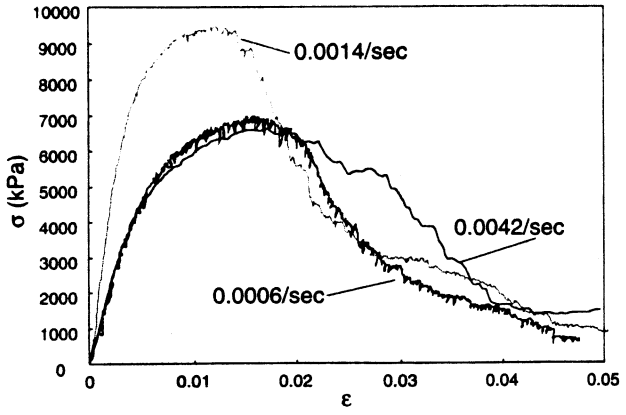

Fig. 9(*a*)

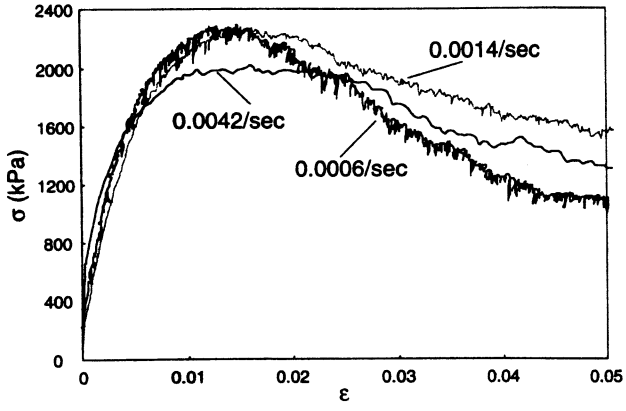

Fig. 9(*b*)

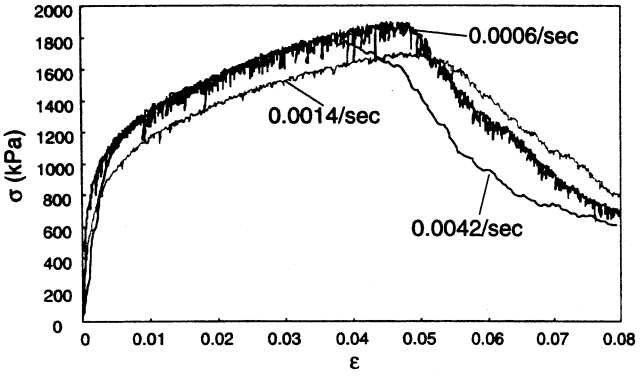

Fig. 9(*c*)

Fig. 9 Representative load-deflection curves for as-received materials tested at several strain rates, showing relative insensitivity to this parameter, for (*a*) material #1, (*b*) material #2, and (*c*) material #3

post-cycled materials. Representative curves for each condition are shown for materials 1, 2, and 3, respectively, in Figs. 10(*a*), (*b*), and (*c*). Average values are summarized in Table 2.

The results show that transverse compression of porous fibrous substrates resulted in higher moduli and peak stresses, as expected. However, electrochemical cycling of the cells resulted in increases in both moduli and peak stresses of the substrate materials, for all types, when cells were run in compressed conditions. This result runs counter to the common hypothesis of swelling damage in the uncompressed condition; namely, that breakdown of the network (be it a sinter, foam or fibrous material) caused by formation of lower-density NiOOH species in the positive plate results in conductive losses and mechanical losses. Here, running cells in corrosive conditions (i.e. overcharge) which would promote low-density phase formation, resulted in generally increased mechanical properties, verifying an earlier, more limited study by the authors.

Material Composition. Specimens in all conditions were studied using a Hitachi S3200 N variable pressure scanning electron microscope, using x-ray energy dispersive spectrometry (XEDS). In these assays, particles and fibers in the networks were studied separately, to determine the composition of each (assuming that composition might depend upon morphology, due to different manufacturing techniques). Results for composition by weight are shown in Table 3. In all materials studied, for each condition and morphology, material compositions were largely independent of morphology and condition.

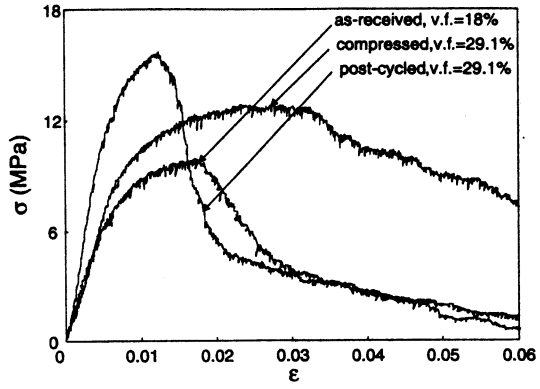

Fig. 10(*a*)

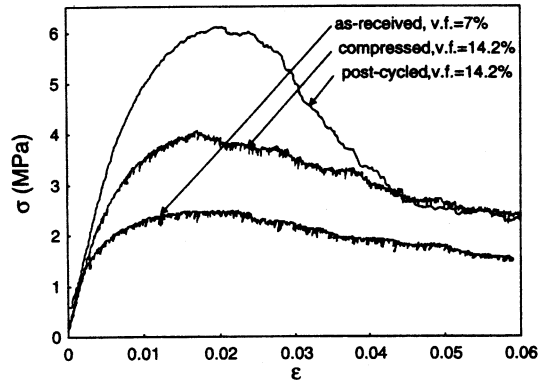

Fig. 10(*b*)

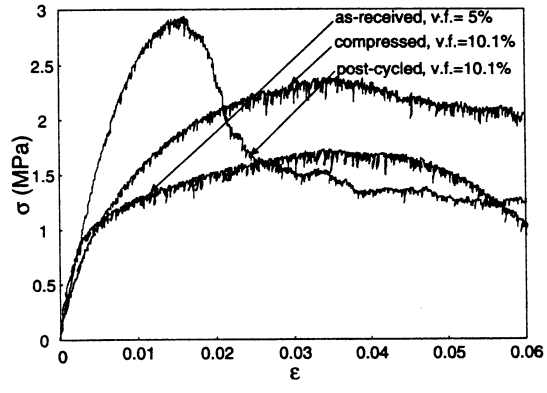

Fig. 10(*c*)

Fig. 10 Representative load-deflection curves obtained for each of three material conditions, respectively: as-received, compressed to approximate cycling thickness in cell, and post-cycled (40 constant current, 150% overcharge cycles). Plots are shown from each condition, for each material: (*a*) material #1, (*b*) material #2, and (*c*) material #3.

Fig. 11(*a*)

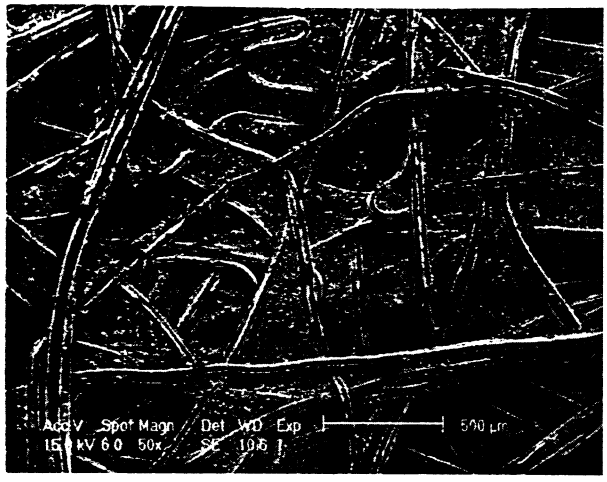

Fig. 11(*b*)

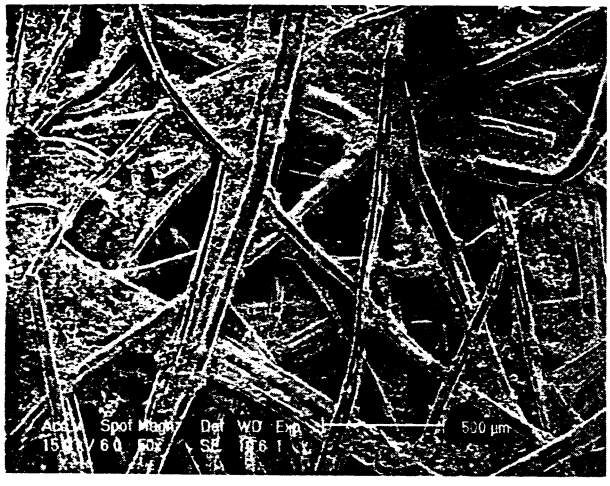

Fig. 11(*c*)

Fig. 11 Scanning electron micrographs of positive plate substrates in the (*a*) as-received condition, (*b*) compressed to the post-cycled volume fraction (~29%), and (*c*) post-cycled (40 constant current cycles and 150% overcharge) condition, for material #1

III Discussion

The simultaneous increase in resistivity, and increase in both modulus and peak load, from the compressed condition to the post-cycled condition cannot be explained simply by breakdown of the bonds in the network. This might be described as sequential damage progression, by, for example, locally high mechanical loads exceeding bond strength in successive bonds, reducing connectivity and ultimately producing a more compliant, weaker and less conductive material. Additional changes in material properties or material morphology were thus examined as possible explanations.

Table 3 Material composition, by weight percent, of substrate constituents (fibers and particles) for all materials in compressed and post-cycled conditions, respectively

	Material 2 (14.2%)				Material 2 (14.2%)				Material 3 (10.1%)			
	Compressed		Post-cycled		Compressed		Post-cycled		Compressed		Post-cycled	
Element	Fiber	Particle	Fiber	Particle	Fiber	Particle	Fiber	Particle	Fiber	Particle	Fiber	Particle
Ni	96.94	100	95.42	100	94.79	100	94.69	100	100	100	100	100
Fe	1.84	0	3.34	0	4.07	0	3.90	0	0	0	0	0
Co	1.22	0	1.24	0	1.17	0	1.41	0	0	0	0	0

Qualitative Image Analysis Via SEM. Scanning electron images of the three materials in each of the three conditions discussed were taken at a number of sections in the substrate materials. Typical examples are shown for materials 1, 2, and 3 in Figs. 11, 12, and 13, respectively. In each case, the effect of compression can be seen clearly as increasing the density of fibers and particles in the image (compare Figs. 11(*a*), 12(*a*), and 13(*a*) with Figs. 11(*b*), 12(*b*), and 13(*b*), respectively). Though it is impossible to discern the overall effect of compression on the state of bonds in the networks from such 2D images, mechanical evidence suggests that generally, mechanical properties are improved with compression. This, in turn, suggests that deformation does not seriously compromise the internal structure. It is possible that compression does cause some bond failure, but these effects are mitigated in mechanical tests by the effect of additional fiber entanglement at higher densities.

Qualitative assessment of SEM images of post-cycled versus the transversely compressed materials (Figs. 11(*b*), 12(*b*), and 13(*b*) with Figs. 11(*c*), 12(*c*), and 13(*c*)) reveals a change in substrate morphology upon cycling. Though these materials have the same overall volume fraction and dimensions (verified experimentally), the distribution of nickel mass is altered: the post-cycled materials exhibit significant loss of interconnected particulate mass, replaced by particulates bonded to the main fibrous network.

Corrosion Processes in the NiMH Cell. This effect, corrosion in NiMH cells caused by electrodeposition of nickel on the positive plate, explains much of the observed behavior. On the negative plate the conversion of MH to M is thermodynamically more favorable than the conversion of Ni to Ni^{2+}; thus, nickel is unlikely to be oxidized on the negative plate. This protects the nickel mesh on the negative plate from being consumed after repeated electrochemical cycling, and ensures sustained conductivity of the negative electrode. Oxidation, however, is favored on the positive plate.

During discharge, NiOOH is reduced to nickel hydroxide ($Ni(OH)_2$) on the positive plate (e.g., Linden, 1995), as

$$NiOOH + H_2O + e \rightarrow Ni(OH)_2 + OH^- \quad E^0 = -0.52V \quad (2)$$

On the negative plate during discharge, the metal hydride MH is oxidized to the metal alloy M (ibid.), as

$$MH + OH^- \rightarrow M + H_2O + e \quad E^0 = -0.83V \quad (3)$$

A simultaneous nickel oxidization process can also occur during discharge on the positive plate (Lide, 1997), as

$$Ni + 2OH^- \rightarrow Ni(OH)_2 + 2e^- \quad E^0 = -0.72V \quad (4)$$

In each reaction, the standard potential [E^0, also referred "single potential" (West, 1970) or "standard reduction potential" (Lide, 1997)] is a measure of the tendency of the chemical reaction,

relative to a zero potential assigned to the $H_2/H^+(aq)$ reaction. On the positive plate, the standard potential of the oxidation Ni to Ni^{2+} transformation is higher than the standard potential for the reduction of Ni^{3+} to Ni^{2+}; thus, oxidization of nickel initiates when a small crack opens on the active material-coated-nickel positive substrate. As more active material is consumed, more surface area

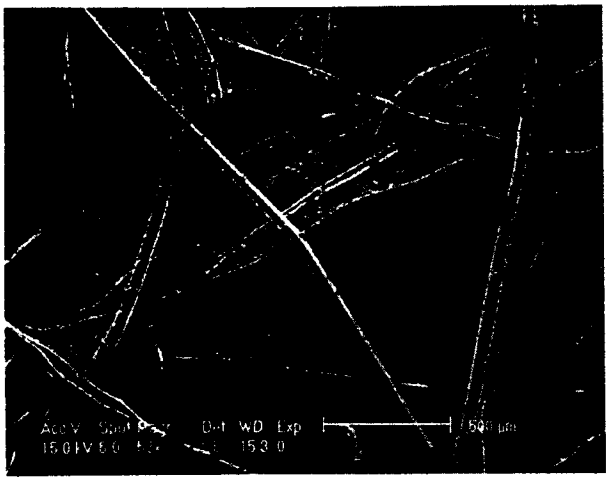

Fig. 12(*a*)

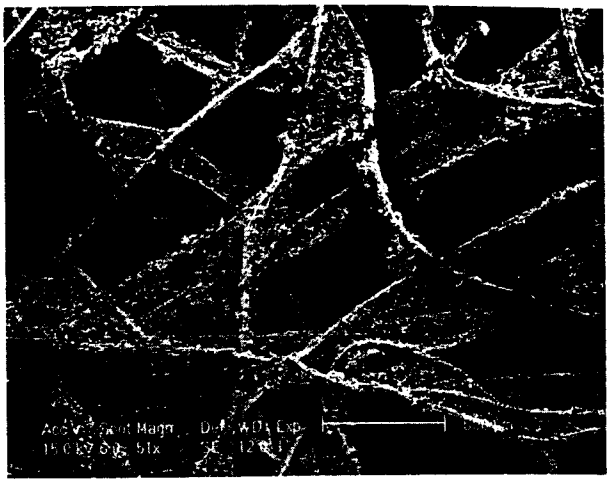

Fig. 13(*a*)

Fig. 12(*b*)

Fig. 13(*b*)

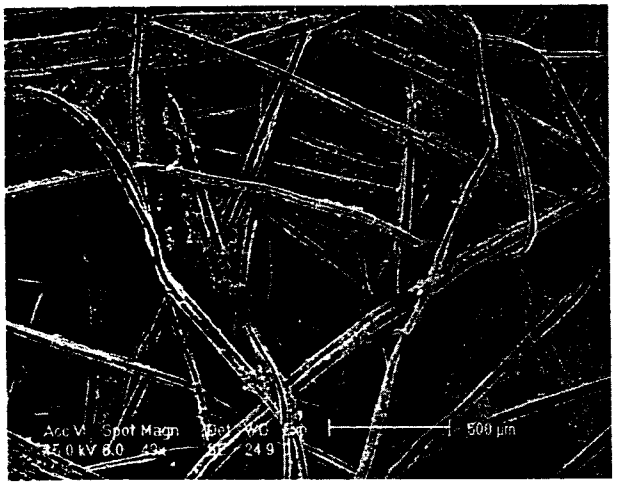

Fig. 12(*c*)

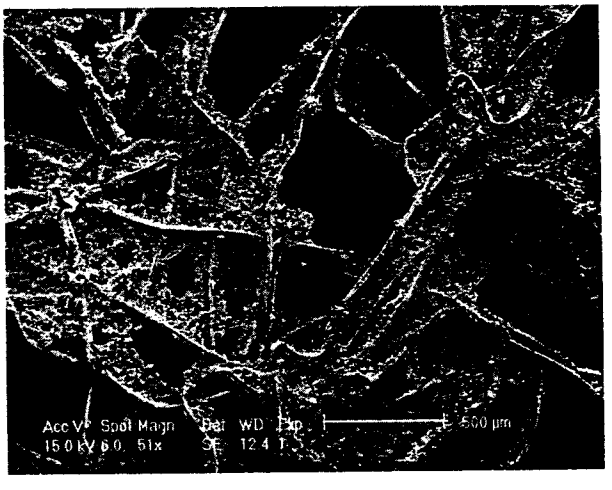

Fig. 13(*c*)

Fig. 12 Scanning electron micrographs of positive plate substrates in the (*a*) as-received condition, (*b*) compressed to the post-cycled volume fraction (~14%), and (*c*) post-cycled (40 constant current cycles and 150% overcharge) condition, for material #2

Fig. 13 Scanning electron micrographs of positive plate substrates in the (*a*) as-received condition, (*b*) compressed to the post-cycled volume fraction (~10%), and (*c*) post-cycled (40 constant current cycles and 150% overcharge) condition, for material #3

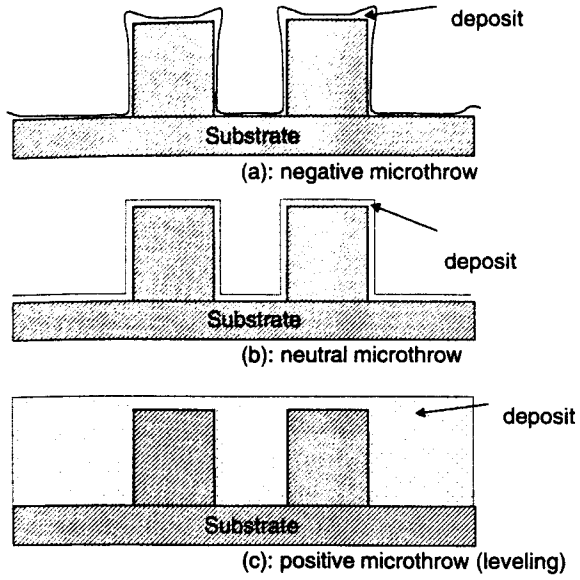

Fig. 14 Deposition of material over model surfaces via electroless plating (adapted from Bunshah, 1994). In (*a*), a "negative microthrow" type process is pictured, where deposited material grows dedritically; (*b*) illustrates a "neutral microthrow" type process, in which surfaces are evenly covered; and (*c*) shows a "positive microthrow" type process, where a rough surface is smoothed by deposited metal.

of the nickel substrate is exposed to electrolyte and surrounding electrons, to form Ni^{2+}. The experiments described here were performed with a substrate comprised of a 50/50 nickel fiber/particle ratio, staple lengths from 0.635 cm–1.905 cm and fiber (particle) diameter of 20–30 μm. The surface area provided by nickel powder, therefore, was 1.5 greater than that of the nickel fibers. Diffused mass is proportional to surface area (e.g., Linden, 1995), and thus the preferential loss of substrate mass via particle consumption is expected.

Charge and especially overcharge recovers part or all of the Ni^{2+} back into the Ni form, depending on the depth of overcharge, with overcharge resulting in higher conversion (Curtis, 1999). The recovered Ni then is deposited onto the nickel substrate. The growth morphology of this electrodeposition can thus be described as follows:

1) Layers of deposited metal form on surfaces, in three general types of morphology as described by Bunshah (1994) and illustrated in Figs. 14(*a–c*). These three types result in collection of deposited material preferentially on convex features (Fig. 14(*a*)), evenly over all features (Fig. 14(*b*)), and preferentially on concave features (Fig. 14(*c*)). In the first case, growth depends mainly on the diffusion of depositing metal ions, causing nodular, dendritic growth depending upon current distribution and local concentration in the diffusion layer (West, 1970). In the last case, the rate of movement of surface-active addition agents is diffusion-limited, and thus there is a leveling of the surface.
2) Because of the preferential consumption of small particles during discharge, the remaining structure (upon which nickel is deposited) is mainly comprised of the lower surface area/volume microstructures, i.e., fibers. Deposition of nickel on the positive substrate thus results in formation of thicker nickel fibers, connected by relatively larger bonds (Figs. 14(*b, c*)).

Active materials used in this study were commercial materials, in which the exact concentrations of species were unknown. However, examination of the SEM images of substrate morphology, coupled with the known effects of electrodeposition on the positive plate, point to an evolution hypothesis for these materials. Namely, that particle mass is consumed in the electrochemical reactions on the positive plate, with overcharge of the cells leading to a redeposition primarily in the form of Fig. 14(*c*). A schematic of this evolution hypothesis is shown in Figs. 15(*a*) and (*b*). The second paper in this series involves simulations on approximations of each condition, and comparison with experimental results, with additional assumptions about material properties.

IV Conclusions and Future Work

An earlier result, that electrochemical cycling at overcharge of NiMH cells produced substrate materials with reduced conductivity, but enhanced mechanical properties, has been verified with more extensive experimentation.

The evolution hypothesis presented here, supported by electrochemical analysis and morphological assays, provides only a guideline for the late-cycle substrate properties. Mass transfer on the substrate and the details of the rate of the corrosion process in

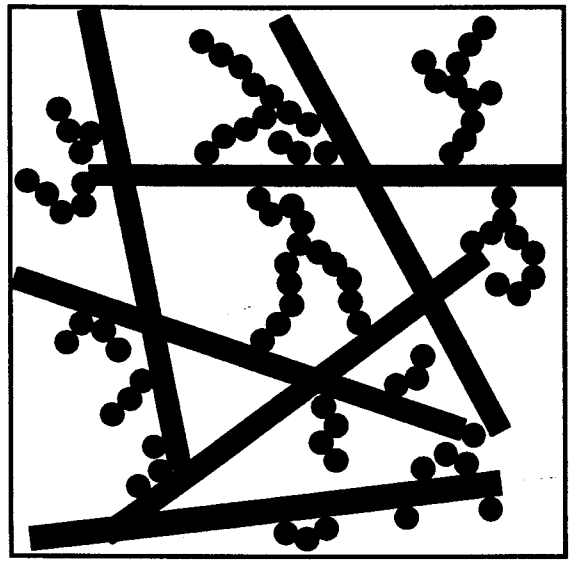

Fig. 15(*a*)

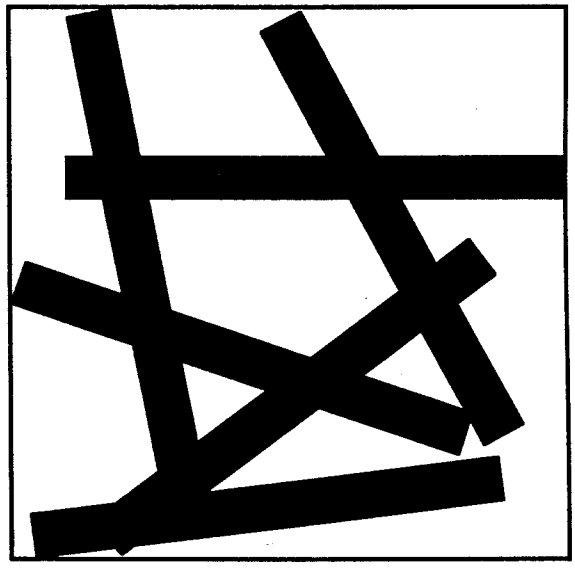

Fig. 15(*b*)

Fig. 15 Evolution hypothesis for morphology of the positive plate. Small nickel particles in the as-received material (*a*), which are thought to form an interconnected network with the fibers, are consumed in the electrochemical reaction and redeposited on the substrate (*b*)

different materials systems and cycling conditions must be assessed. This is complicated by the number of materials reacting in the positive plate, which includes active material, electrolyte and the substrate material itself. Our observations showed evidence of mass transfer from the nickel particulate form to the fiber network, but did not suggest further mass transfer, i.e., fibers in the materials imaged appeared to be intact. More extensive changes in morphology could be expected under more severe cycling conditions. Capacity losses associated in part with these morphological changes were somewhat higher for higher-density substrates, though all values were small.

Results here, along with results of prior work, do suggest that the morphological changes alone would dramatically affect conduction in substrates. Distribution of mass in higher aspect-ratio fiber networks is favorable to conduction, particularly at low volume fractions, because of enhanced connectivity (Cheng and Sastry, 1999; Cheng et al., 1999a, b). In design of superior substrate materials, these changes must be anticipated and designed for, to achieve good conductivity in the positive plate, and long-life cells.

Acknowledgments

This work was supported by the Lawrence Berkeley Laboratories, through the Exploratory Research Program of the U.S. Department of Energy. Helpful comments on electrochemical mechanisms were provided by Professor M. David Curtis, University of Michigan. Additional support and materials were provided by Mr. Robert Hellen and Mr. Tom Kelly, of Yardney Technical Products, Pawcatuck, CT: Ms. Susan Herczeg of National Standard; and Mr. Marshall Muller at Ovonic Battery Company. Support provided by an NSF PECASE grant is also gratefully acknowledged.

References

Bunshah, R. F., 1994, *Handbook of Deposition Technologies for Films and Coatings*, Noyes Publication, Park Ridge, NJ, pp. 494–499.

Cheng, X., and Sastry, A. M., 1999, "On Transport in Stochastic, Heterogeneous Fibrous Domains," to appear, *Mechanics of Materials*.

Cheng, X., Sastry, A. M., and Layton, B. E., 1999a, "Transport in Stochastic Fibrous Networks," in preparation, ASME JOURNAL OF ENGINEERING MATERIALS AND TECHNOLOGY.

Cheng, X., Wang, C. W., Sastry, A. M., and Choi, S. B., 1999b, "Investigation of Failure Processes in Porous Battery Substrates: Part II—Simulation Results and Comparisons," ASME JOURNAL OF ENGINEERING MATERIALS AND TECHNOLOGY, published in this issue pp.

Coates, D., Paul, G., and Daugherty, P., 1990, "Advances in Lightweight Nickel Electrode Technology," *Journal of Power Sources*, Vol. 29, pp. 521–529.

Curtis, D., 1999, personal communication.

Davolio, G., Da Pieve, A., and Soragni, E., 1989, "On the Mechanical Properties of Nickel Oxide Electrodes," *Proceedings of the Symposium on Nickel Hydroxide Electrodes*, Hollywood, FL, pp. 281–295.

Ferrando, W. A., 1992, "Fabrication of Prototype Large Scale Composite Fiber Nickel Electrodes," *The 35th International Power Sources Symposium*, pp. 141–144.

Ferrando, W. A., Lee, W. W., and Sutula, R. A., 1984, "A Lightweight Nickel Composite Electrode I: Concept and Feasibility," *Journal of Power Sources*, Vol. 12, No. 3–4, pp. 249–265.

Fritts, D. H., 1981, "Testing the Mechanical Characteristics of Sintered Nickel Battery Plaque and Their Relationship to Nickel Electrode Performance," *Journal of Power Sources*, Vol. 6, pp. 171–184.

Fritts, D. H., 1984, "Estimation of the Mechanical Stress in Nickel Electrode Sinter and its Implications for Nickel Electrode Construction," *Journal of Power Sources*, Vol. 12, No. 3–4, pp. 267–275.

Hellen, R., 1999, Personal Communication.

Lide, R. D., editor-in-chief, 1997, *CRC Handbook of Chemistry & Physics*, 1997–1998, 78th edition, CRC Press, 8–23.

Muller, M., 1997, Personal Communication.

Linden, D., editor-in-chief, 1995, *Handbook of Batteries*, second edition, McGraw-Hill, New York, pp. 2.4/2.16/33.2–33.3.

Oshitani, M., Takayama, T., Takashima, K., and Tsuji, S., 1986, "A Study on the Swelling of Sintered Nickel Hydroxide Electrode," *Journal of Applied Electrochemistry*, Vol. 16, pp. 403–412.

Sastry, A. M., Wang, C. W., and Cheng, X., 1998a, "Mechanics of Stochastic Fibrous Networks," *Journal of Thermoplastic Composite Materials*, Vol. 30, pp. 288–296.

Sastry, A. M., Cheng, X., and Choi, S. B., 1998b, "Damage in Composite NiMH Positive Electrodes," ASME JOURNAL OF ENGINEERING MATERIALS AND TECHNOLOGY, Vol. 120, pp. 280–283.

Sastry, A. M., 1994, "Modeling Conductivity of Composite Substrates for Nickel-Metal Hydride Batteries," Sandia Report SAND94-2884.

Tatarchuk, B. J., 1994, "Composite Fiber Structures for Catalysts and Electrodes," *Journal of Power Sources*, Vol. 47, pp. 297–302.

USABC, 1996, "USABC Electric Vehicle Battery Test Procedures Manual, Revision 2," principal author: Gary Hunt, Idaho National Engineering Laboratory (INEL), U.S. Department of Energy Idaho Field Office, DOE/ID-10479, Rev. 2.

West, J. M., 1970, *Electrodeposition and Corrosion Processes*, Van Nostrand Reinhold, London, U.K., pp. 123–124.